Article

Operando studies reveal active Cu nanograins for CO_2 electroreduction

https://doi.org/10.1038/s41586-022-05540-0

Received: 17 March 2022

Accepted: 8 November 2022

Check for updates

Yao Yang[1,2,3,11], Sheena Louisia[1,3,11], Sunmoon Yu[3,4,11], Jianbo Jin[1], Inwhan Roh[1,3], Chubai Chen[1,3], Maria V. Fonseca Guzman[1,3], Julian Feijóo[1,3], Peng-Cheng Chen[1,5], Hongsen Wang[6], Christopher J. Pollock[7], Xin Huang[7], Yu-Tsun Shao[8], Cheng Wang[9], David A. Muller[8,10], Héctor D. Abruña[6,10] & Peidong Yang[1,3,4,5]✉

Carbon dioxide electroreduction facilitates the sustainable synthesis of fuels and chemicals[1]. Although Cu enables CO_2-to-multicarbon product (C_{2+}) conversion, the nature of the active sites under operating conditions remains elusive[2]. Importantly, identifying active sites of high-performance Cu nanocatalysts necessitates nanoscale, time-resolved operando techniques[3–5]. Here, we present a comprehensive investigation of the structural dynamics during the life cycle of Cu nanocatalysts. A 7 nm Cu nanoparticle ensemble evolves into metallic Cu nanograins during electrolysis before complete oxidation to single-crystal Cu_2O nanocubes following post-electrolysis air exposure. Operando analytical and four-dimensional electrochemical liquid-cell scanning transmission electron microscopy shows the presence of metallic Cu nanograins under CO_2 reduction conditions. Correlated high-energy-resolution time-resolved X-ray spectroscopy suggests that metallic Cu, rich in nanograin boundaries, supports undercoordinated active sites for C–C coupling. Quantitative structure–activity correlation shows that a higher fraction of metallic Cu nanograins leads to higher C_{2+} selectivity. A 7 nm Cu nanoparticle ensemble, with a unity fraction of active Cu nanograins, exhibits sixfold higher C_{2+} selectivity than the 18 nm counterpart with one-third of active Cu nanograins. The correlation of multimodal operando techniques serves as a powerful platform to advance our fundamental understanding of the complex structural evolution of nanocatalysts under electrochemical conditions.

Copper remains the only heterogeneous electrocatalyst to selectively catalyse the CO_2 reduction reaction (CO_2RR) to multicarbon (C_{2+}) products, including ethylene, ethanol and propanol, at appreciable rates[1,2]. Recent developments in operando/in situ methods, including advanced electron microscopy and synchrotron-based X-ray, provide powerful nondestructive tools to probe active sites and structural changes of electrocatalysts under reaction conditions[3–5]. However, there remains a lingering debate over the active state of Cu catalysts regarding valence state or coordination environments under CO_2RR. For instance, some reports have proposed Cu^+ species and subsurface oxide as potential active sites of oxide-derived Cu electrocatalysts[6–9] whereas others have suggested that the active state of bulk Cu catalysts is metallic[10–12], because subsurface oxides are not stable under negative potentials[13–15]. Another potential structural descriptor of locally enhanced CO_2RR activity reported is micrometre-sized grain boundaries on bulk metal electrodes[13–18]. Those studies probed local activity at grain boundaries at micrometre-level spatial resolution, suitable only for bulk electrodes. Because C_{2+} product formation involves a C–C coupling step over multiple atomic Cu sites in close proximity[2], resolving catalytically active sites at or close to subnanometre resolution is necessary to uncover the structural origin of CO_2RR-active surfaces. In particular, operando methods with high spatiotemporal resolution are instrumental in elucidating active sites of Cu nanoparticle (NP) electrocatalysts (under 100 nm) among many other nanocatalysts[19].

Building on our previous studies, this study presents a comprehensive structural picture of the life cycle for a family of high-performance Cu NP ensemble electrocatalysts and provides a baseline understanding of their structures[20–22]. An ensemble of monodisperse Cu NPs underwent a structural transformation process (that is, 'electrochemical scrambling') where the surface oxide is reduced, followed by ligand desorption and formation of aggregated/disordered Cu structures that correlate with the formation of catalytically active sites for CO_2RR (Fig. 1a). The active Cu structures rapidly evolve into single-crystal Cu_2O nanocubes on exposure to air. Herein, we propose that active Cu nanograins play a critical role in the reduction/oxidation life cycle of these Cu nanocatalysts: (1) active sites for selective reduction of CO_2 to C_{2+} products and (2) highly reactive sites for breaking O=O bonds and insertion of O atoms in the tetrahedral sites of Cu lattice.

[1]Department of Chemistry, University of California, Berkeley, CA, USA. [2]Miller Institute for Basic Research in Science, University of California, Berkeley, CA, USA. [3]Chemical Sciences Division, Lawrence Berkeley National Laboratory, Berkeley, CA, USA. [4]Department of Materials Science and Engineering, University of California, Berkeley, CA, USA. [5]Kavli Energy NanoScience Institute, Berkeley, CA, USA. [6]Department of Chemistry and Chemical Biology, Cornell University, Ithaca, NY, USA. [7]Cornell High Energy Synchrotron Source, Cornell University, Ithaca, NY, USA. [8]School of Applied and Engineering Physics, Cornell University, Ithaca, NY, USA. [9]Advanced Light Source, Lawrence Berkeley National Laboratory, Berkeley, CA, USA. [10]Kavli Institute at Cornell for Nanoscale Science, Cornell University, Ithaca, NY, USA. [11]These authors contributed equally: Yao Yang, Sheena Louisia, Sunmoon Yu. ✉e-mail: p_yang@berkeley.edu

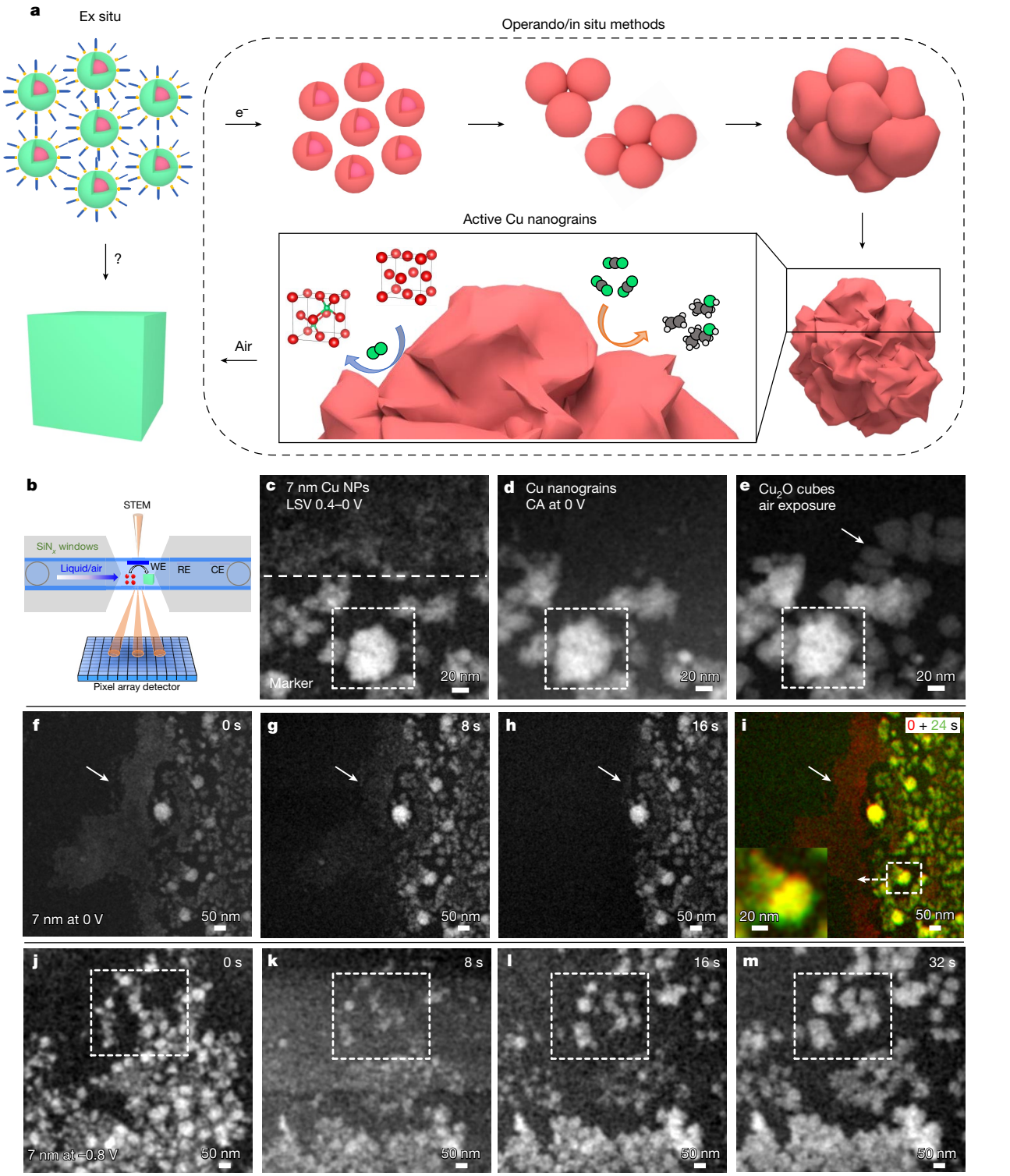

Fig. 1 | Scheme of the life cycle of Cu nanocatalysts and operando EC-STEM studies of dynamic morphological changes of 7 nm NPs. a, While conventional ex situ methods are limited to the study of nanocatalysts before/after CO_2RR, the operando/in situ methods used in this study uncover the dynamic changes in morphology, composition and structure under real-time catalytically relevant conditions. An ensemble of monodisperse Cu NPs undergo structural transformation during which the surface oxide is reduced, ligands are desorbed and a progressive coalescence/aggregation leads to the formation of active metallic Cu nanograins. We propose that these highly polycrystalline Cu nanograins are made of disordered grain boundaries that support undercoordinated Cu active sites for C_{2+} formation. On exposure to air, Cu nanograins also demonstrate high reactivity for O_2 bond breakage and insertion in the Cu lattice to form Cu_2O. **b**, Schematic of operando EC-STEM and 4D-STEM with the capability of enabling quantitative electrochemical measurements and simultaneous tracking of morphological and structural changes under CO_2RR-relevant conditions. **c**–**e**. Overview of the life cycle of 7 nm Cu nanocatalysts shown by EC-STEM images of initial growth after a single negative-direction LSV scan, from 0.4 to 0 V (**c**), further growth under CA at 0 V (**d**) and the post-electrolysis formation of Cu_2O cubes (marked by the arrow) when exposed to air at the same location (**e**). **f**–**i**, Morphological evolution of 7 nm NPs at 0 V versus RHE at 0 (**f**), 8 (**g**), 16 (**h**) and 24 s (**i**). False-colour images in the inset of (**i**) highlight newly formed regions (green) after 24 s growth. **j**–**m**, Further particle aggregation of 7 nm NPs at −0.8 V for 0 (**j**), 8 (**k**), 16 (**l**) and 32 s (**m**), with significant changes highlighted in dashed boxes.

A family of Cu NP (7, 10 and 18 nm) ensembles was studied to investigate size dependence on their structural evolution dynamics. High-angle annular dark-field scanning transmission electron microscopy (HAADF–STEM) images show synthesized Cu NPs with narrow size distribution (Supplementary Fig. 1). Atomic-scale STEM images and corresponding electron energy loss spectroscopy (EELS) mapping of as-synthesized fresh 7 nm NPs show a Cu@Cu_2O core-shell structure with a metallic Cu core surrounded by an oxide shell of approximately 2 nm (Extended Data Fig. 1a,b and Supplementary Fig. 2). The 7 nm Cu NPs oxidized to Cu_2O NPs after air exposure for over 5 h post synthesis (Supplementary Figs. 3 and 4). We note that, whether 7 nm NPs are partially or fully oxidized, this does not impact catalytic performance because they probably reach a comparable active state during electrolysis (Supplementary Fig. 4). By contrast, both 10 and 18 nm NPs maintain a stable Cu@Cu_2O core-shell structure over extended air exposure, suggesting that a minimum particle size of around 10 nm is required to form a self-passivated surface oxide layer (Extended Data Fig. 1c–f and Supplementary Figs. 6–10). This ex situ analysis of pristine Cu nanocatalysts provides the necessary guidance for further operando electrochemical STEM (EC-STEM) studies.

To track the dynamic morphological and structural evolution of Cu nanocatalysts and elucidate the nature of Cu active sites, we used operando EC-STEM and four-dimensional STEM (4D-STEM) diffraction imaging. The operando EC-STEM cell encapsulates a liquid pocket with a three-electrode configuration, including Cu NPs deposited on the carbon working electrode, Pt counter and Pt pseudoreference electrode (WE, CE and RE, respectively)[23–25] (Fig. 1b). The redox potential and current density measured in the operando EC-STEM cell indicate that Cu NPs electrochemically behave consistently with standard H-cell measurements (Supplementary Figs. 11–13). A potential of −0.8 V versus reversible hydrogen electrode (RHE; all potentials are referenced to the RHE scale unless noted otherwise) was applied on the 7 nm NPs ensemble in the EC-STEM cell to simulate the optimal CO_2RR potential for C_{2+} product formation (Supplementary Fig. 14). The as-prepared EC-STEM cell has a liquid thickness of 500 nm or greater[26], which is often too thick to resolve NPs below 10 nm (Supplementary Fig. 15). Thus we adopted a 'thin liquid' strategy[27,28], performing a single linear sweep voltammetry (LSV) scan from 0.4 to 0 V to trigger the hydrogen evolution reaction (typically co-existent during CO_2RR). Electrogenerated H_2 bubbles enable a thinner liquid film of about 100 nm, as quantified by liquid-cell EELS (Supplementary Fig. 16), leading to a significantly enhanced spatial resolution for tracking of individual NPs in liquids (Supplementary Fig. 17 and Supplementary Video 1). We observed that parts of the NP ensemble (lower part below the dashed line) already experienced noticeable particle aggregation immediately after the LSV scan (Fig. 1c). This points to the high reactivity/mobility of small Cu NPs even at potentials more positive than the onset of the CO_2RR (−0.4 V). Operando EC-STEM images captured at 0 V at an identical location show marked aggregation of the remaining 7 nm NPs into Cu nanograins with sizes of 50–100 nm (Fig. 1d,e). On exposure to air, small Cu nanograins (under 50 nm) evolved into Cu_2O nanocubes whereas some large Cu nanoclusters (over 100 nm) maintained an irregular morphology, possibly because of the loss of reactivity of bulk Cu with O_2[22]. Figure 1c–e provides an overview of the electroreduction/oxidation life cycle of the 7 nm Cu NP ensemble.

To resolve the initial stage of Cu nanograin formation, a mild potential of 0 V was applied on the 7 nm NP ensemble (Fig. 1f–i). Operando EC-STEM videos in this study were first recorded without applied potentials as control experiments to ensure that no beam-induced damage had occurred (Supplementary Video 2). After the initial LSV scan, Cu nanograins were observed and the remaining 7 nm Cu NPs underwent rapid structural transformation, leading to the formation of new Cu nanograins and additional particle growth (Fig. 1f–h). A false-colour STEM image taken at 0 and 24 s (red versus green) illustrates the difference, with the image in the inset highlighting the particle growth process on existing Cu nanograins (Fig. 1i and Supplementary Fig. 18). At the C_{2+} optimal potential (−0.8 V), more marked particle movement occurred in the first 8 s followed by progressive particle aggregation/coalescence (8–32 s) (Fig. 1j–m and Supplementary Video 3). Cu nanograins of 50–100 nm formed at −0.8 V approached a steady-state structure after extended electroreduction for 90 s (Supplementary Fig. 19). Following airflow, Cu nanograins rapidly evolved into well-defined Cu_2O nanocubes of around 100 nm, similar to those formed after H-cell measurement (Supplementary Figs. 20 and 21). In summary, operando EC-STEM of the 7 nm Cu NP ensemble identified two types of morphology: loosely connected small Cu nanograins and closely packed large Cu nanograins, which may serve as active sites for CO_2RR.

Operando 4D-STEM diffraction imaging in liquid provides unique structural information beyond the traditional STEM imaging of morphological changes[27]. 4D-STEM uses a newly developed electron microscope pixel array detector (EMPAD) that can rapidly record a two-dimensional (2D) electron diffraction pattern over a 2D grid of probe positions[29–32]. 4D-STEM, with its high sensitivity and dynamic range, can significantly lower electron dose while retrieving nanometre-scale crystallographic information, which is indispensable for beam-sensitive materials in liquid. We focus on the structural transformation of the most active 7 nm NPs from the initial stage to the steady state of Cu nanograins, followed by post-electrolysis Cu_2O nanocubes formed following air exposure (Fig. 2, left). The HAADF–STEM image in Fig. 2a shows 7 nm, NP-derived, loosely connected Cu nanograins formed at 0 V. A virtual bright-field (BF) STEM image, retrieved from 4D-STEM datasets, better shows the fine granular features of Cu nanograins (Fig. 2b). One particular domain (Fig. 2c) was selected to show the diffraction pattern of a metallic Cu domain with Cu{111} (2.1 Å) and Cu{200} (1.8 Å) close to the Cu[110] zone axis. 4D-STEM dark-field imaging, based on diffraction spots 1 (red), 2 (green) and 3 (blue), yielded a false-colour map showing crystal domains with the same/similar crystal orientations resembling those three diffraction spots. The 4D-STEM composite maps in Fig. 2d clearly show the highly polycrystalline nature of active Cu with fine nanograins. Two particular regions highlight those nanograin boundaries that are either loosely connected (Fig. 2e) or closely overlapped (Fig. 2f). The Cu grains shown in Fig. 2e,f are around 5–10 nm, comparable to the size of pristine 7 nm Cu NPs. This indicates that pristine 7 nm Cu NPs serve as building blocks in the formation of nanograin boundaries, which are probably rich in defects and dislocations after the initial stage of electroreduction at 0 V. Similar metallic Cu nanograins were widely observed in other 4D-STEM maps (Supplementary Fig. 22). To the best of our knowledge, this observation represents the first report of sub-10 nm nanograin boundaries supporting possible Cu active sites, at an unprecedented spatial resolution enabled by a probe size of approximately 1 nm.

Following electroreduction at −0.8 V, metallic Cu nanograins (50–100 nm) achieved a steady-state, closely packed structure (Fig. 2g). A majority of diffraction patterns from Cu domains indicate polycrystalline metallic Cu (Fig. 2h), with few domains showing a single-crystal-like metallic Cu feature close to the Cu[110] zone axis (Fig. 2i). This indicates that some Cu nanograins have sufficient driving force for reconstruction into highly crystalline Cu domains during electroreduction at −0.8 V. False-colour dark-field 4D-STEM maps, based on the three diffraction spots shown in Fig. 2i, show that the majority of Cu nanograins are composed of individual grains separated by grain boundaries and/or stacking faults (Fig. 2j, white arrows). Interestingly, the Cu nanograins magnified in the dashed box in Fig. 2j show the predominant crystal orientation in green resembling diffraction spot 2 in Fig. 2i, and some metallic Cu nanograins on the surface with other crystal orientations in red resembling diffraction spot 1. This in-depth structural analysis indicates that the dominant active Cu sites, formed at −0.8 V, are closely packed and highly polycrystalline metallic Cu nanograins relative to the loosely connected Cu nanograins formed at 0 V.

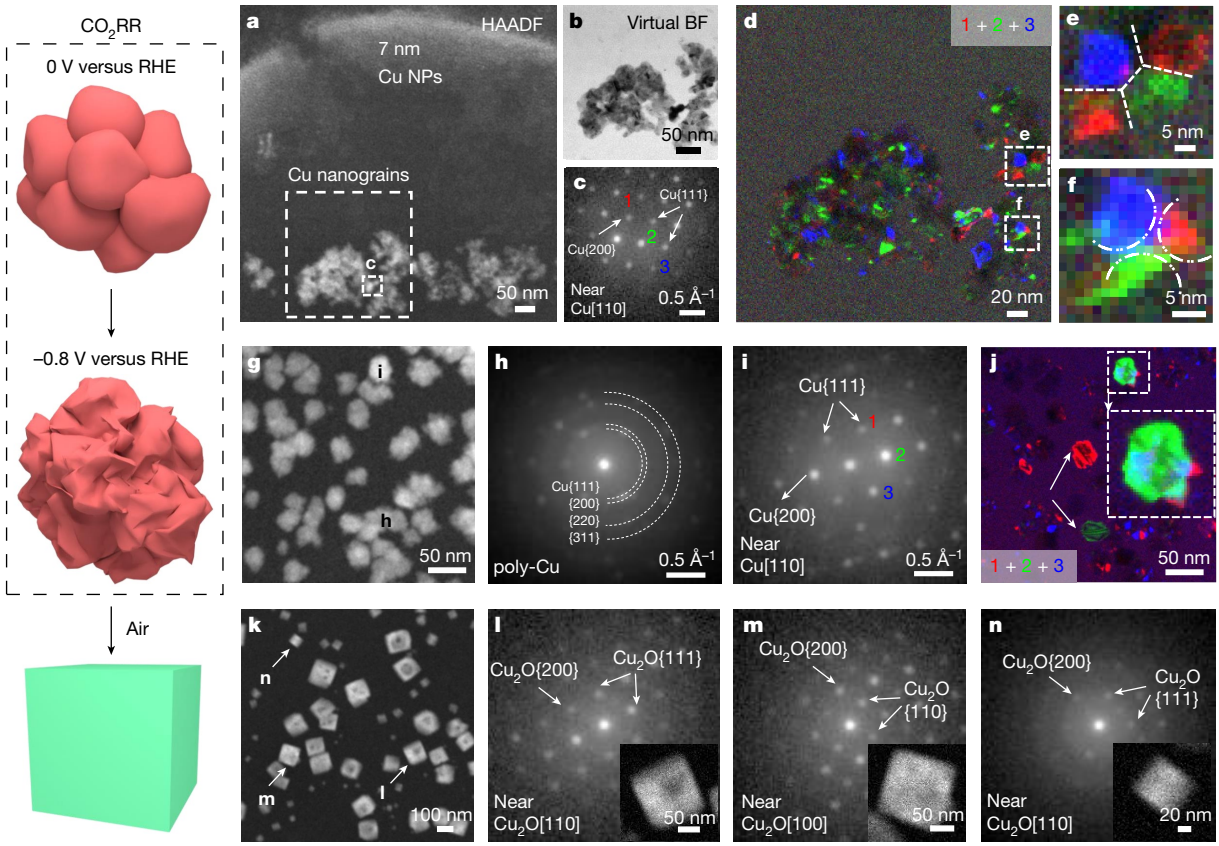

Fig. 2 | Operando 4D-STEM diffraction imaging of metallic Cu nanograins. **a**–**n**, Left, scheme serving as a visual guide to the structural evolution, from the initial stage of loosely connected Cu nanograins at 0 V (**a**–**e**) to steady-state closely packed Cu nanograins at −0.8 V (**g**–**i**), followed by the formation of Cu_2O cubes when exposed to air (**k**–**n**). **a**, HAADF–STEM images of co-existing 7 nm NPs and loosely connected active Cu nanograins following initial growth at 0 V. **b**, Virtual BF STEM image of Cu nanograins reconstructed from 4D-STEM datasets from the dashed box in **a**. **c**, Representative electron diffraction pattern of one Cu domain in **a** showing the metallic Cu with Cu{200} (1.8 Å) and Cu{111} (2.1 Å) close to the [110] zone axis. **d**, False-colour dark-field 4D-STEM maps showing Cu nanograins with diffraction spots resembling those in **b** marked as 1 (red), 2 (green) and 3 (blue), respectively. **e**,**f**, Two particular regions, extracted from the dashed box in **d**, showing loosely connected Cu nanograins (**e**) and overlapping nanograin boundaries (**f**). **g**, HAADF–STEM image of closely packed Cu nanograins formed at −0.8 V. **h**,**i**, Representative diffraction patterns of highly polycrystalline Cu (poly-Cu) (**h**) and single-crystal-like Cu nanograins (**i**). **j**, False-colour dark-field 4D-STEM maps showing highly crystalline Cu nanograins with diffraction spots resembling those three marked as 1, 2 and 3 in **i**. **k**, HAADF–STEM image of Cu_2O nanocubes formed on air exposure. **l**–**n**, Selective diffraction patterns of single-crystal Cu_2O cubes with d-spacings of {200} (2.1 Å), {111} (2.5 Å) or {110} (3.0 Å).

Under airflow to repel electrolytes, metallic Cu nanograins at the same location in the EC-STEM cell rapidly evolved into well-defined Cu_2O nanocubes (Fig. 2k). The 4D-STEM diffraction patterns in Fig. 2l–n show that the Cu_2O nanocubes are single crystals with edge length of around 60–120 nm. We hypothesize that metallic Cu nanograins formed under bias are highly defective/disordered, rendering them especially reactive to O_2 molecules. O=O bonds can dissociate and allow the spontaneous insertion of O atoms in the Cu lattice. In addition, operando EC-STEM of post-synthesis Cu_2O nanocubes under bias shows the fragmentation of large cubes (about 100 nm) and redeposition of small nanoclusters (under 20 nm), which is markedly different from the structure of metallic Cu nanograins (50–100 nm) formed at −0.8 V (Supplementary Fig. 23 and Supplementary Video 4). This suggests that metallic Cu nanograins can be derived only from the 7 nm Cu NP ensemble and cannot be reversibly obtained from post-electrolysis Cu_2O nanocubes. As demonstrated by the loss of C_{2+} selectivity/activity on utilization of these post-electrolysis nanocubes (Supplementary Fig. 24), only metallic Cu nanograins obtained through the assembly and reconstruction of self-assembled Cu NPs can serve as the supporting structure for CO_2RR-active undercoordinated Cu sites. In summary, operando EC-STEM suggests that the 7 nm Cu NP ensemble evolves into polycrystalline/disordered Cu nanograins and transforms into single-crystal Cu_2O nanocubes post electrolysis.

Similar to 7 nm NPs, 10 nm NPs underwent substantial particle movement/aggregation during the first 8 s at −0.8 V and continued to grow into larger Cu nanograins (50–100 nm) (Fig. 3a–d, Supplementary Figs. 25 and 26 and Supplementary Video 5). Meanwhile, the 18 nm Cu NP ensemble showed a distinctly different structural evolution. After an initial LSV to 0 V, 18 nm Cu NPs on the carbon WE partially aggregated and formed intriguing 'melting' features at the initial stage (Fig. 3e,f). Subsequent air exposure led to the transformation of metallic nanograins into well-defined Cu_2O nanocubes whereas nearby unreacted 18 nm Cu NPs remained unchanged (Fig. 3g and Supplementary Fig. 27). At −0.8 V, 18 nm Cu NPs underwent progressive particle reconstruction and migration (Fig. 3i–k) and agglomerated into large Cu nanograins after around 4 min (Supplementary Fig. 28 and Supplementary Video 6). The limited and slower structural reconstruction of the larger NPs probably originates from their intrinsically lower surface energy; additionally, larger NPs are packed less closely due to restricted interdigitation of their surface ligands in comparison with the smaller NP ensemble[33,34]. As a result, the initial aggregation of 10 and 18 nm Cu NPs is less dramatic than that of 7 nm Cu NPs, leading to a lower density of nanograin boundaries and less active undercoordinated Cu sites. This hypothesis is corroborated by Pb underpotential deposition (UPD) that indicates a higher density of undercoordinated sites on the 7 nm Cu NP ensemble (Supplementary Fig. 29).

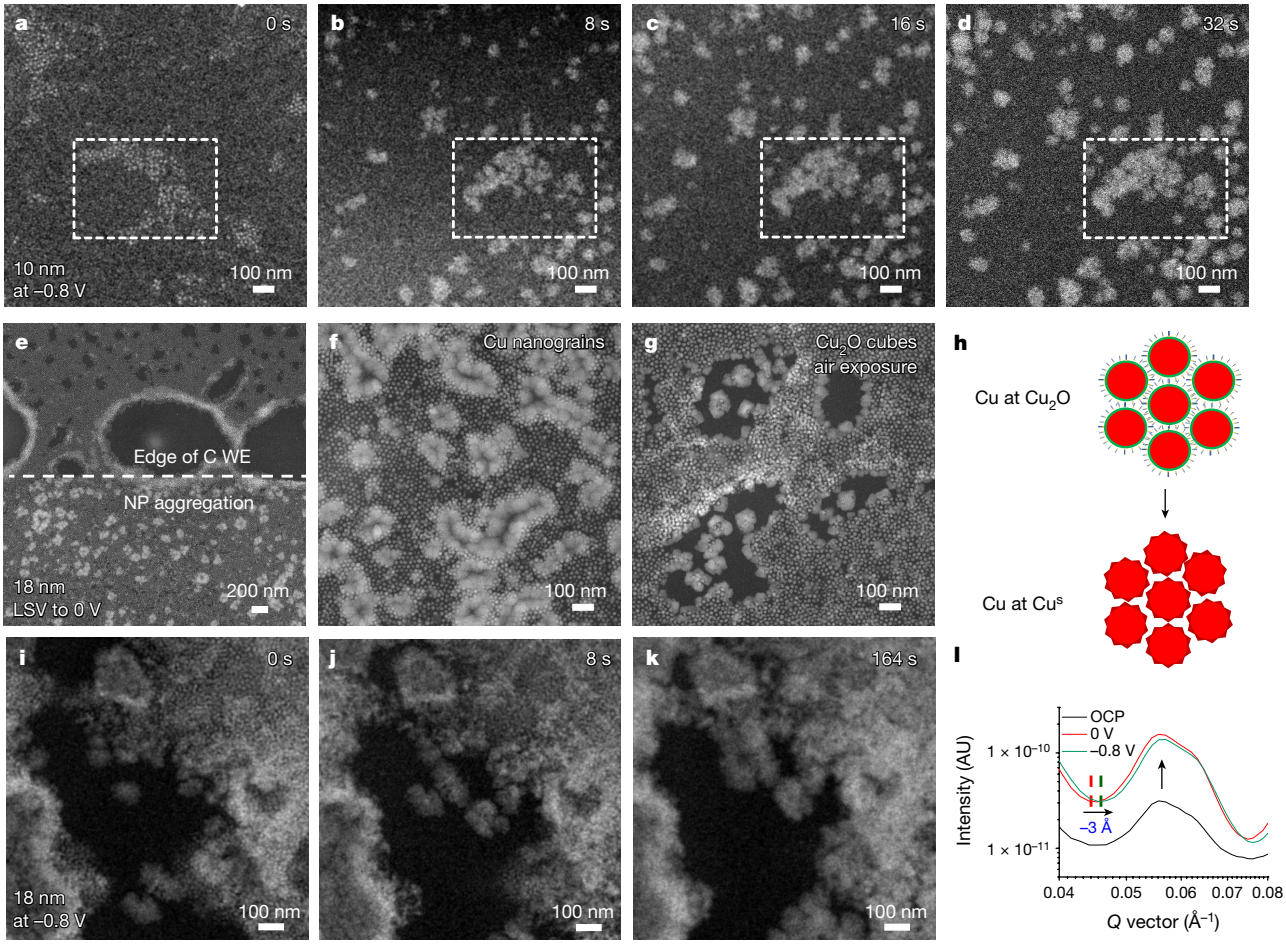

Fig. 3 | Operando EC-STEM studies of dynamic morphological changes in 10 and 18 nm NPs. a–**d**, Selected operando EC-STEM video frames of the evolution of 10 nm NPs at −0.8 V at 0 (**a**), 8 (**b**), 16 (**c**) and 32 s (**d**). **e**,**f**, EC-STEM images showing 18 nm NPs partially melted into Cu nanograins after initial growth following one LSV scan from 0.4 to 0 V. Limit of NP aggregation (**e**) and Cu nanograins (**f**). **g**, STEM image of Cu_2O nanocubes formed from Cu nanograins following exposure to air, with nearby unreacted 18 nm NPs maintaining their pristine morphology. **h**,**l**, Structural models showing the transformation from 18 nm Cu NP ensembles to metallic Cu nanograins with surface Cu sites (Cu@Cu^s) (**h**) and average grain size smaller than pristine NPs by around 3 Å (**l**), which was supported by operando RSoXS studies using the same liquid-cell TEM holder. **i**–**k**, Operando EC-STEM images of the slower dynamic evolution of 18 nm NPs relative to 7 nm NPs at −0.8 V for 0 (**i**), 8 (**j**) and 164 s (**k**) relative to 7 nm NPs. AU, arbitrary units.

The particle aggregation dynamics of 18 nm Cu NPs are illustrated in the structural model in Fig. 3h. We posit that the surface oxide of 18 nm Cu NPs is reduced and that NPs form metallic Cu nanograins with surface-active sites (Cu@Cu^s) in a more closely packed structure. This hypothesis is supported by operando resonant soft X-ray scattering (RSoXS)[34] using the same liquid-cell set-up as operando EC-STEM (Fig. 3l). At 0 V, the X-ray scattering intensity of Cu increased dramatically relative to the pristine 18 nm Cu NP ensembles measured at open circuit potential (OCP). This indicates a higher level of aggregation of Cu NPs per unit area leading to stronger X-ray scattering, which is consistent with the formation of the denser melting feature in EC-STEM (Fig. 3f). At −0.8 V the X-ray intensity remained at a similar level but exhibited a noticeable shift of the first minimum to a higher *Q*-value, which corresponds to an average grain size smaller than that of pristine 18 nm Cu NPs, by 2.9 ± 0.2 Å (one monolayer) (Supplementary Fig. 30). This suggests that, although 18 nm Cu NPs, as building blocks, aggregated to form active Cu nanograins, only the surface 2 nm oxide layer participated in formation of a lower density of nanograin boundaries, thus resulting in a smaller contribution of active undercoordinated Cu sites. Operando RSoXS provides a statistically robust analysis of the aggregation dynamics of Cu NPs, complementing the operando EC-STEM studies.

Operando high-energy-resolution fluorescence detected X-ray absorption spectroscopy (HERFD-XAS) was then used to elucidate the valence state and coordination environment of the Cu NP ensemble under CO_2RR conditions and following exposure to air (Fig. 4). The electrochemical behaviour of Cu nanocatalysts was comparable in both the customized X-ray cell and H-cell, with no observation of beam damage on the Cu NPs in electrolyte (Supplementary Figs. 31–33). HERFD-XAS enables a significantly higher energy resolution (approximately 1 eV) than conventional solid-state fluorescence detection (50–200 eV)[10–12,35,36], enabling the detection of fine features in X-ray absorption near-edge spectroscopy (XANES) pre-edge regions (Supplementary Figs. 34–36). HERFD-XANES of the 7 nm Cu NP ensemble showed the same pre-edge energy as bulk Cu_2O (Fig. 4a), supporting the view that NPs are fully oxidized after storage in air as previously shown by EELS (Supplementary Fig. 3). The chemical state of Cu NPs was then investigated under CO_2RR. At −0.8 V, the NP ensemble showed edge features similar to those of Cu foil. The observed transition to metallic Cu is consistent with the formation of the Cu nanograins observed with 4D-STEM (Fig. 2). On post-electrolysis air exposure, the NPs completely re-oxidized to Cu_2O. The resolution of HERFD-XANES enabled us to carry out accurate quantitative analysis of the valence states achieved throughout the NP life cycle (Supplementary Figs. 37–39). The oxide volume fractions of NP ensembles, as determined by XAS, are consistent with oxide shell thickness in EELS analysis (Supplementary Fig. 40). Quantitative valence analysis over the course of electrolysis showed

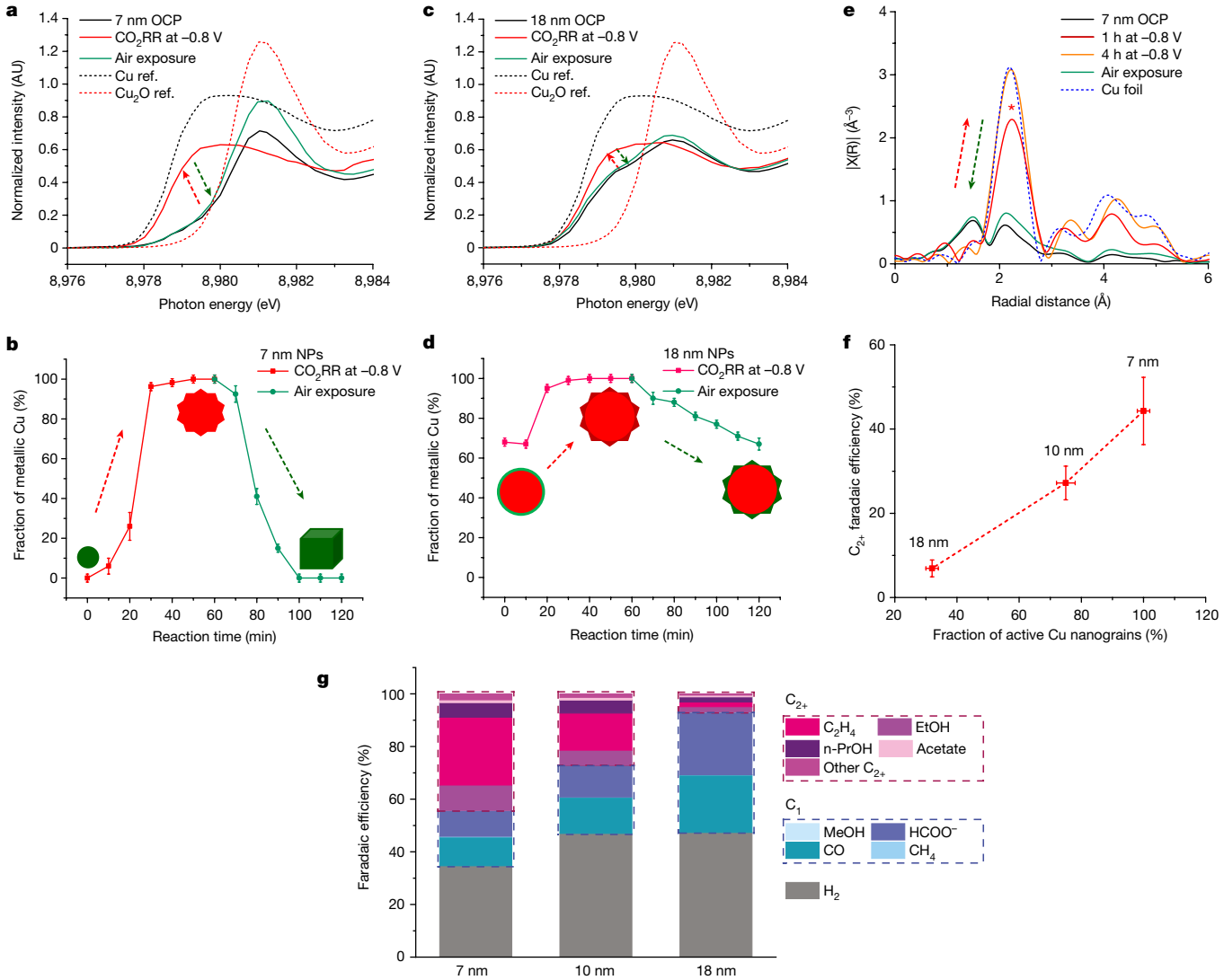

Fig. 4 | Operando HERFD-XAS study of the valence state and coordination environment of Cu nanocatalysts during their electroreduction/reoxidation life cycle. a, Operando HERFD-XANES spectra of pristine 7 nm NPs, metallic Cu formed at −0.8 V under CO_2RR conditions and Cu_2O cubes formed following post-electrolysis exposure to air, along with the standard references (ref.) of bulk Cu and Cu_2O (dashed lines). **b**, Quantitative analysis of relative fraction of metallic Cu, showing conversion from Cu_2O NPs to fully metallic Cu nanograins and reoxidation of Cu nanograins to Cu_2O nanocubes following exposure to air. **c**,**d**, Operando HERFD-XANES (**c**) and corresponding quantitative analysis (**d**) of 18 nm NPs at −0.8 V showing transformation from Cu@Cu_2O NPs to fully metallic Cu nanograins and reoxidation of those Cu nanograins to mixed phases of Cu/Cu_2O following exposure to air. The electroreduction/reoxidation cycle was confined to the surface oxide layer. **e**, Operando HERFD-EXAFS of 7 nm NPs under CO_2RR conditions and following exposure to air, with EXAFS after 1 h of electroreduction, suggesting the presence of undercoordinated Cu sites as highlighted by the red asterisk. |X(R)| is the EXAFS amplitude. **f**, Structure–activity correlation of relative fraction of active Cu nanograins and C_{2+} faradaic efficiency of Cu NP ensembles with three different NP sizes. **g**, Faradaic efficiency for all CO_2RR products grouped as C_{2+}, C_1 products and H_2 obtained from ensembles of three different Cu NP sizes (7, 10 and 18 nm) at −0.8 V in an H-cell.

the metallic Cu fraction increasing from 0 to 100% over 1 h (Fig. 4b and Supplementary Fig. 41), which was corroborated by second-level tracking of electroreduction/oxidation kinetics at constant photon energy (Supplementary Figs. 42 and 43). These measurements testify that electroreduction of the 7 nm Cu NPs was completed within around 30 min at −0.8 V.

HERFD-XANES of 18 nm Cu NPs indicated an average composition of around 70% metallic Cu in the core and around 30% Cu_2O in the shell. These larger NPs underwent a similar transition to metallic Cu under electroreduction, although less marked relative to the smaller NPs (Fig. 4c and Supplementary Fig. 44). In addition, the pre-edge peak after post-electrolysis exposure to air suggested that 18 nm Cu NPs evolved into a mixed Cu and Cu_2O phase, matching the partial formation of nanocubes from EC-STEM studies (Fig. 3g). Quantitative valence analysis suggested that the electroreduction of 18 nm Cu NPs was confined to the surface Cu_2O layer and required a shorter time (approximately 10 min) than their 7 nm NP counterparts (around 30 min), whereas the partial reoxidation of metallic Cu occurred progressively over 1 h (Fig. 4d and Supplementary Fig. 45).

Given that all three types of Cu NP ensembly (7, 10 and 18 nm) show complete conversion from partially/fully oxidized pristine NPs to fully metallic Cu nanograins (Supplementary Figs. 37, 45 and 46), the fraction of active Cu nanograins is defined as the relative fraction of the pristine Cu NP ensemble that can be converted to metallic Cu active sites under electrochemical potentials (Fig. 4f). This quantitative value was then correlated to the CO_2RR performance of the different Cu NP ensembles (Fig. 4f,g and Supplementary Tables 1 and 2). The resulting structure–activity correlation suggests that a higher fraction of

active Cu nanograins leads to higher C_{2+} selectivity. In particular, the 7 nm Cu NP ensemble with 100% Cu nanograins shows a C_{2+} selectivity sixfold higher than that of the 18 nm Cu NP ensemble, with only 32% Cu nanograins at −0.8 V. The activity and stability of these nanograins was also tested in a gas diffusion electrode (GDE) in which the 7 nm Cu NP ensemble showed a higher C_{2+} faradaic efficiency of (~57%) at a much higher current density of 300 mA cm^{-2} relative to the H-cell (~44%) at 15 mA cm^{-2} (Supplementary Table 3). This demonstrates that 7 nm Cu NP-derived nanograins can also perform under industrially relevant conditions.

Further EXAFS analysis of the Cu NP ensembles provides additional details on their active structure (Fig. 4e and Supplementary Figs. 47–50). The scattering amplitude of the Cu–Cu peak for 7 nm Cu NPs after 1 h of electroreduction was markedly lower than that of the standard Cu foil (Fig. 4e). Specifically, EXAFS fitting of the nanocatalyst after 1 h of CO_2RR yielded an average nearest Cu–Cu coordination number (CN) of approximately 8, suggesting the presence of undercoordinated Cu sites (Supplementary Fig. 50). Eventually, after 4 h of electroreduction the Cu–Cu CN approached a steady-state value of 12, comparable to that of Cu foil. Such an increase probably resulted from the continuous aggregation/coalescence of smaller Cu nanograins into fully grown Cu nanograins (50–100 nm), with a negligible contribution from undercoordinated surface Cu sites[37] (Supplementary Fig. 47). We hypothesize that whereas surface and bulk Cu become spectroscopically indistinguishable, because EXAFS is more sensitive to bulk than surface, undercoordinated sites are still present within the steady-state structure of the Cu nanocatalysts. This is corroborated by Pb UPD measurements indicating the presence of stronger binding sites formed on the 7 nm Cu NP ensemble (Supplementary Fig. 29).

Although our EXAFS results suggest that the slow structural change in the NP ensemble would lead to variation in nanocatalyst catalytic activity, we note that only the signal obtained after 4 h is associated with the catalyst steady-state structure. Such slow kinetics result from the operando X-ray cell configuration and are otherwise much faster in the H-cell, as demonstrated by CO_2RR activity becoming stabilized within 20 min and maintained for 4 h and beyond (Supplementary Fig. 51). We further narrow down the time frame when the Cu NP ensemble structural transformation leads to the formation of C–C coupling active sites with operando differential electrochemical mass spectrometry (DEMS) measurements at high temporal resolution, enabled by a dual thin-layer flow cell[38]. Specifically, C_2H_4 production reaches a steady state within the first 2.5 s in a DEMS flow-cell configuration, which is sufficiently fast compared with the time of around 20 min necessary to reach the steady-state structure and C_2H_4 production in an H-cell (Supplementary Fig. 52). The early-stage C_{2+} production demonstrated by DEMS ties in with the formation of Cu nanograins observed within the first few seconds under applied potentials in the EC-STEM cell. Meanwhile, the steady-state structure identified by operando XAS can be correlated to steady-state activity measured in the H-cell (Supplementary Fig. 51). Overall, we can chronologically establish a structure–activity correlation that confirms the catalytic significance of undercoordinated sites supported on Cu nanograins relevant to C_{2+} production.

In summary, this correlated operando structural studies with electron of the electroreduction/reoxidation life cycle of Cu nanocatalysts. Metallic Cu nanograins, rich in grain boundaries, support a high density of active undercoordinated sites that enhances the C_{2+} selectivity of the 7 nm Cu NP ensemble. This study represents a milestone towards spatially resolving the complex nature of active Cu sites for CO_2RR. Further statistical analysis of grain boundary density[13,39], grain–grain distance[40] and relative grain orientations[24] will provide additional insights on which structural factors of Cu nanograins are beneficial to C_{2+} formation. Inspired by the active formation of Cu nanograins via rapid NP evolution, various approaches can be devised to utilize such structural transformation to generate nanocatalysts with higher C_{2+} intrinsic activity. For instance, smaller nanoparticles, clusters or molecular complexes can be used as smaller building blocks to generate a higher density of nanograin boundaries supporting undercoordinated active Cu sites. As proof of concept, a smaller-sized Cu NP ensemble (about 5 nm) was synthesized and demonstrated markedly higher C_{2+} selectivity (55%) at lower Cu mass loading relative to the 7 nm counterpart (44%) (Supplementary Note, Supplementary Figs. 53–57, Supplementary Video 7 and Supplementary Table 4). We anticipate that correlation of operando structural studies with electron and X-ray probes and additional molecular-level spectroscopical methods will be necessary to unravel which intermediates bind and undergo C–C coupling on the active sites supported on those nanograin boundaries. This study emphasizes the importance and prospects of using correlative operando methods in contributing to the rational design of future nanoscale electrocatalysts.

Online content

Any methods, additional references, Nature Portfolio reporting summaries, source data, extended data, supplementary information, acknowledgements, peer review information; details of author contributions and competing interests; and statements of data and code availability are available at https://doi.org/10.1038/s41586-022-05540-0.

1. Ross, M. B. et al. Designing materials for electrochemical carbon dioxide recycling. *Nat. Catal.* **2**, 648–658 (2019).
2. Birdja, Y. Y. et al. Advances and challenges in understanding the electrocatalytic conversion of carbon dioxide to fuels. *Nat. Energy* **4**, 732–745 (2017).
3. Yang, Y. et al. *Operando* methods in electrocatalysis. *ACS Catal.* **11**, 1136–1178 (2021).
4. Mefford, J. T. et al. Correlative operando microscopy of oxygen evolution electrocatalysts. *Nature* **593**, 67–73 (2021).
5. Vavra, J., Shen, T. H., Stoian, D., Tileli, V. & Buonsanti, R. Real-time monitoring reveals dissolution/redeposition mechanism in copper nanocatalysts during the initial stages of the CO_2 reduction reaction. *Angew. Chem. Int. Ed. Engl.* **60**, 1347–1354 (2021).
6. Hahn, C. et al. Engineering Cu surfaces for the electrocatalytic conversion of CO_2: controlling selectivity toward oxygenates and hydrocarbons. *Proc. Natl Acad. Sci. USA* **114**, 5918–5923 (2017).
7. Li, C. W., Ciston, J. & Kanan, M. W. Electroreduction of carbon monoxide to liquid fuel on oxide-derived nanocrystalline copper. *Nature* **508**, 504–507 (2014).
8. Arán-Ais, R. M., Scholten, F., Kunze, S., Rizo, R. & Roldan Cuenya, B. The role of in situ generated morphological motifs and Cu(i) species in C_{2+} product selectivity during CO_2 pulsed electroreduction. *Nat. Energy* **5**, 317–325 (2020).
9. Eilert, A. et al. Subsurface oxygen in oxide-derived copper electrocatalysts for carbon dioxide reduction. *J. Phys. Chem. Lett.* **8**, 285–290 (2017).
10. Chang, C.-J. et al. Dynamic reoxidation/reduction-driven atomic interdiffusion for highly selective CO_2 reduction toward methane. *J. Am. Chem. Soc.* **142**, 12119–12132 (2020).
11. Kimura, K. W. et al. Selective electrochemical CO_2 reduction during pulsed potential stems from dynamic interface. *ACS Catal.* **10**, 8632–8639 (2020).
12. Li, J. et al. Copper adparticle enabled selective electrosynthesis of n-propanol. *Nat. Commun.* **9**, 4614 (2018).
13. Lum, Y. & Ager, J. W. Stability of residual oxides in oxide-derived copper catalysts for electrochemical CO_2 reduction investigated with ^{18}O labeling. *Angew. Chem. Int. Ed. Engl.* **57**, 551–554 (2018).
14. Fields, M., Hong, X., Nørskov, J. K. & Chan, K. Role of subsurface oxygen on Cu surfaces for CO_2 electrochemical reduction. *J. Phys. Chem. C* **122**, 16209–16215 (2018).
15. Garza, A. J., Bell, A. T. & Head-Gordon, M. Is subsurface oxygen necessary for the electrochemical reduction of CO_2 on copper? *J. Phys. Chem. Lett.* **9**, 601–606 (2018).
16. Feng, X., Jiang, K., Fan, S. & Kanan, M. W. A direct grain-boundary-activity correlation for CO electroreduction on Cu nanoparticles. *ACS Cent. Sci.* **2**, 169–174 (2016).
17. Mariano, R. G., McKelvey, K., White, H. S. & Kanan, M. W. Selective increase in CO_2 electroreduction activity at grain-boundary surface terminations. *Science* **358**, 1187–1192 (2017).
18. Mariano, R. G. et al. Microstructural origin of locally enhanced CO_2 electroreduction activity on gold. *Nat. Mater.* **20**, 1000–1006 (2021).
19. Yang, Y. et al. Electrocatalysis in alkaline media and alkaline membrane-based energy technologies. *Chem. Rev.* **122**, 6117–6321 (2022).
20. Hung, L., Tsung, C.-K., Huang, W. & Yang, P. Room-temperature formation of hollow Cu_2O nanoparticles. *Adv. Mater.* **22**, 1910–1914 (2010).
21. Kim, D., Kley, C. S., Li, Y. & Yang, P. Copper nanoparticle ensembles for selective electroreduction of CO_2 to C_2–C_3 products. *Proc. Natl Acad. Sci. USA* **114**, 10560–10565 (2017).
22. Li, Y. et al. Electrochemically scrambled nanocrystals are catalytically active for CO_2-tomulticarbons. *Proc. Natl Acad. Sci. USA* **117**, 9194–9201 (2020).
23. Holtz, M. E. et al. Nanoscale imaging of lithium ion distribution during in situ operation of battery electrode and electrolyte. *Nano Lett.* **14**, 1453–1459 (2014).
24. Yang, Y., Shao, Y.-T., Lu, X., Abruña, H. D. & Muller, D. A. Metal monolayers on command: underpotential deposition at nanocrystal surfaces: a quantitative *operando* electrochemical transmission electron microscopy study. *ACS Energy Lett.* **7**, 1292–1297 (2022).

25. Williamson, M., Tromp, R., Vereecken, P., Hull, R. & Ross, F. Dynamic microscopy of nanoscale cluster growth at the solid–liquid interface. *Nat. Mater.* **2**, 532–536 (2003).
26. Holtz, M. E., Yu, Y., Gao, J., Abruña, H. D. & Muller, D. A. *In situ* electron energy-loss spectroscopy in liquids. *Microsc. Microanal.* **19**, 1027–1035 (2013).
27. Yang, Y., Shao, Y.-T., Lu, X., Abruña, H. D. & Muller, D. A. Elucidating cathodic corrosion mechanisms with *operando* electrochemical transmission electron microscopy. *J. Am. Chem. Soc.* **144**, 15698–15708 (2022).
28. Serra-Maia, R. et al. Nanoscale chemical and structural analysis during in situ scanning/transmission electron microscopy in liquids. *ACS Nano* **15**, 10228–10240 (2021).
29. Chen, Z. et al. Electron ptychorgraphy achieves atomic-resolution limits set by lattice vibrations. *Science* **372**, 826–831 (2021).
30. Tate, M. W. et al. High dynamic range pixel array detector for scanning transmission electron microscopy. *Microsc. Microanal.* **22**, 237–249 (2016).
31. Ophus, C. Four-dimensional scanning transmission electron microscopy (4D-STEM): from scanning nanodiffraction to ptychography and beyond. *Micro. Microanal.* **25**, 563–582 (2020).
32. Zuo, J. M. & Tao, J. in *Scanning Transmission Electron Microscopy* (eds Pennycook, S. & Nellist, P.) Ch. 9 (Springer, 2011).
33. Yu, S. et al. Nanoparticle assembly induced ligand interactions for enhanced electrocatalytic CO_2 conversion. *J. Am. Chem. Soc.* **143**, 19919–19927 (2021).
34. Yang, Y. et al. *Operando* resonant soft X-ray scattering studies of chemical environment and interparticle dynamics of Cu nanocatalysts for CO_2 electroreduction. *J. Am. Chem. Soc.* **144**, 8927–8931 (2022).
35. Glatzel, P. & Bergmann, U. High resolution 1s core hole X-ray spectroscopy in 3D transition metal complexes-electronic and structural information. *Coord. Chem. Rev.* **249**, 65–95 (2005).
36. Yang, Y. et al. *In situ* X-ray absorption spectroscopy of a synergistic Co-Mn oxide catalyst for the oxygen reduction reaction. *J. Am. Chem. Soc.* **141**, 1463–1466 (2019).
37. Reske, R., Mistry, H., Behafarid, F., Roldan Cuenya, B. & Strasser, P. Particle size effects in the catalytic electroreduction of CO_2 on Cu nanoparticles. *J. Am. Chem. Soc.* **136**, 6978–6986 (2018).
38. Zeng, R. et al. Methanol oxidation using ternary ordered intermetallic electrocatalysts: a DEMS study. *ACS Catal.* **10**, 770–776 (2020).
39. Cao, L. et al. Mechanistic insights for low-overpotential electroreduction of CO_2 to CO on copper nanowires. *ACS Catal.* **7**, 8578–8587 (2017).
40. Jeong, H. M. et al. Atomic-scale spacing between copper facets for the electrochemical reduction of carbon dioxide. *Adv. Energy Mater.* **10**, 1903423 (2020).

Methods

Synthesis

Copper NPs (7 nm) were synthesized as previously reported by our group[21]. For larger nanoparticles, size was controlled by tuning the mole ratio of tetradecylphosphonic acid to copper(I) acetate (CuAc) precursors, in which higher ratios resulted in larger particles. Specifically, to synthesize 7, 10 and 18 nm NPs, ratios of 0.5, 0.7 and 1.2, respectively, were used while maintaining the absolute concentration of CuAc (1 mmol). Synthesis of 5 nm Cu NPs was adapted from a previously reported hot-injection method[41]. Additional synthesis details can be found in Supplementary Information.

Electrochemical measurements in H-cells

One monolayer of densely packed 7 nm NPs was achieved with a mass loading of 68.9 μg deposited on 1 cm^2 carbon paper (Sigracet 29AA, Fuel Cell Store). The design of the H-cell used in this study was described in detail previously[21,42]. Electrochemical measurements were performed in 0.1 M $KHCO_3$ at a CO_2 flow rate of 20 ml min^{-1} using a Biologic potentiostat, with Cu NPs supported on carbon paper as the WE, Ag/AgCl (3 M KCl) as the RE and Pt wire as the CE, the last of these separated from the WE by an anion exchange membrane (Selemion AMV). All faradaic efficiencies reported herein are normalized whereas those before normalization are in the range 90–100%. Pb UPD measurement was conducted in a solution of 0.1 M $NaClO_4$, 10 mM $HClO_4$ and 3 mM $Pb(II)(ClO_4)_2$(ref. [43]). Additional details about GDE measurements can be found in Supplementary Information.

Operando EC-STEM and 4D-STEM measurements

Operando EC-STEM imaging was performed in CO_2-saturated 0.1 M $KHCO_3$ of regular liquid thickness (500 nm or greater) in a Tecnai F-20 STEM. A Protochips Poseidon liquid-cell holder and Gamry potentiostat were used for electrochemical measurements in EC-STEM. Operando EC-STEM images were acquired at a speed of 4 s per frame (1,024 × 1,024 pixels with a dwell time of 3 μs per pixel) at a beam dose of around 50 e^- nm^{-2} per frame (dose rate of about 12.5 e^- nm^{-2} s^{-1}). This low dose is critical to ensure the absence of beam-induced damage to reliably track electrochemical reactions. A beam dose control experiment was routinely performed before each dynamic video capture to ensure no evidence of beam damage. 4D-STEM experiments were performed using an EMPAD by recording a 2D diffraction pattern at each probe position, resulting in 4D datasets. 4D-STEM diffraction imaging was performed with a probe size of about 1.3 nm in full-width at half-maximum and 256 × 256 pixels at a dose of approximately 2,000 e^- nm^{-2} (dose rate of about 6 e^- nm^{-2} s^{-1}). Additional details can be found in Supplementary Information.

Ex situ STEM and EELS measurement

Ex situ atomic-scale HAADF–STEM imaging and EELS were performed in a fifth-order, aberration-corrected STEM (Nion UltraSTEM) operated at 100 keV with a semiconvergence angle of 30 mrad. EELS spectrum images were acquired with 0.25 eV per channel energy dispersion in a Gatan spectrometer at a size of around 100–200 pixels and an acquisition time of 10–20 ms per pixel. Cu and O elemental maps were extracted using Cu $L_{3,2}$ and O K edges from EELS spectrum images, and processed using principal component analysis and the linear combination of power law to subtract the background in ImageJ software.

Operando HERFD-XAS measurements

Cu K-edge XANES and EXAFS were acquired in HERFD mode at the PIPOXS beamline of the Cornell High Energy Synchrotron Source (CHESS) under ring conditions of 100 mA at 6 GeV. Incident energy was selected using a cryogenically cooled Si(311) monochromator and focused using a pair of Rh-coated mirrors. HERFD-XAS selects one particular fluorescence decay channel, the Cu $K\alpha_1$ emission line at 8,048 eV (refs. [36,37]), by Si{444} single crystals in Rowland geometry. The sample was placed at an angle of 45° relative to the incident beam and fluorescence was detected using a Pilatus 100K detector, enabling the isolation of decay transition from a single orbital with a much longer core hole lifetime. Given the energy–time uncertainty principle, this enables significantly enhanced energy resolution in the order of 1 eV relative to the typical 50–200 eV of a conventional solid-state fluorescence detector. The design of the customized X-ray cell can be found in our previous report[37]. Cu NP catalysts were deposited on carbon paper as the WE with the same Cu loading as H-cell measurements. The RE (Ag/AgCl (saturated KCl)) was placed (via a salt bridge) at the bottom of the cell to minimize iR drop during electrochemical testing. Additional details can be found in Supplementary Information.

Operando RSoXS measurements

Soft X-ray measurements were performed in the same type of liquid-cell set-up (Protochips, Inc.) as the operando EC-STEM holder, with a liquid thickness of about 1 μm. Soft X-ray data were collected at the Advanced Light Source beamline 11.0.1.2 with a back-illuminated Princeton PI-MTE CCD cooled to −45 °C. Scattering patterns of 18 nm NPs were collected for 0.6 s to minimize soft X-ray beam damage. RSoXS data fitting was conducted using the software package Scatter[44].

Operando DEMS measurements

Electrochemical measurements were performed with an EG&G Model 173 potentiostat/galvanostat, an EG&G Model 175 universal programmer and a DEMS set-up. A monolayer of 7 nm NPs on a glassy carbon electrode (diameter, 1.0 cm) served as the working electrode, with a mass loading of 8.14 μg cm^{-2}. Two Pt wires were used as dual counter electrodes to minimize iR drop. A Ag/AgCl (saturated KCl) was used as the reference electrode. DEMS measurements were performed in a dual thin-layer flow cell at a flow rate of 10 μl s^{-1}. A detailed description of the DEMS set-up can be found in our previous work[38].

Data availability

All relevant data are available from the corresponding author on request.

41. Mantella, V. et al. Polymer lamellae as reaction intermediates in the formation of copper nanospheres as evidenced by in situ X-ray studies. *Angew. Int. Chem. Ed. Engl.* **59**, 11627–11633 (2020).
42. Kim, D. et al. Selective CO_2 electrocatalysis at the pseudocapacitive nanoparticle/ordered-ligand interlayer. *Nat. Energy* **5**, 1032–1042 (2020).
43. Sebastián-Pascual, P. & Escudero-Escribano, M. Surface characterization of copper electrocatalysts by lead underpotential deposition. *J. Electroanal. Chem.* **896**, 115446 (2021).
44. Förster, S., Apostol, L. & Bras, W. Scatter: software for the analysis of nano- and mesoscale small-angle scattering. *J. Appl. Crystallogr.* **43**, 639–646 (2010).

Acknowledgements This work was supported by the Director, Office of Science, Office of Basic Energy Sciences, Chemical Sciences, Geosciences, & Biosciences Division of the US Department of Energy under contract nos. DE-AC02-05CH11231 and FWP CH030201 (Catalysis Research Program). Work at Cornell University (in particular, operando EC-STEM) was supported by the Center for Alkaline-Based Energy Solutions, an Energy Frontier Research Center programme supported by the US Department of Energy, under grant no. DE-SC0019445. This work made use of TEM facilities at the CCMR, which are supported through the National Science Foundation Materials Research Science and Engineering Center (NSF MRSEC) programme (no. DMR-1719875). This work also used TEM facilities at the Molecular Foundry, supported by the Office of Science, Office of Basic Energy Sciences of the US Department of Energy under contract no. DE-AC02-05CH11231. This research used resources of the Advanced Light Source, which is a DOE Office of Science User Facility under contract no. DE-AC02-05CH11231. This work is based on research conducted at the Center for High-Energy X-ray Sciences (CHEXS), which is supported by the National Science Foundation under award DMR-1829070. We thank J. Grazul and M. Thomas at Cornell for TEM technical support, and R. Dhall and K. Bustillo at NCEM. We thank H. Celik and UC Berkeley's NMR facility at the College of Chemistry (CoC-NMR) for spectroscopic assistance. Instruments in the CoC-NMR are supported in part by NIH S10OD024998. We thank Y. Li for the initial discussion on in situ TEM. We thank R. Page and S. McFall for X-ray cell fabrication at the machine shop of Cornell LASSP. Y.Y. acknowledges support from the Miller Research Fellowship. S.Y. acknowledges support from the Samsung Scholarship. J.J. and C.C. acknowledge support from the Suzhou Industrial Park Scholarship.

Author contributions Y.Y., S.L. and S.Y. designed the project under the guidance of P.Y. and H.D.A. Y.Y. performed atomic-scale STEM–EELS and operando EC-STEM measurements.

Y.Y. performed operando 4D-STEM, with the help of Y.-T.S. and under the guidance of D.A.M. S.L. and I.R. synthesized Cu nanocatalysts and performed CO_2RR performance measurements, with the help of M.V.F.G. and J.F. S.Y. performed X-ray diffraction analysis and H-cell measurements. I.R. performed GDE measurements. Y.Y. performed operando HERFD-XAS studies, with help from S.L., S.Y. and X.H. C.J.P. provided generous support for the operando HERFD set-up. Y.Y. performed operando RSoXS studies under the guidance of C.W., with help from J.J. and C.C. H.W. and Y.Y. performed operando DEMS measurements. J.J. and C.C. prepared the scheme. Y.Y., S.L. and S.Y. wrote the manuscript under the supervision of P.Y. All authors revised and approved the manuscript.

Competing interests The authors declare no competing interests.

Additional information

Supplementary information The online version contains supplementary material available at https://doi.org/10.1038/s41586-022-05540-0.

Correspondence and requests for materials should be addressed to Peidong Yang.

Peer review information *Nature* thanks Dunfeng Gao and the other, anonymous, reviewer(s) for their contribution to the peer review of this work.

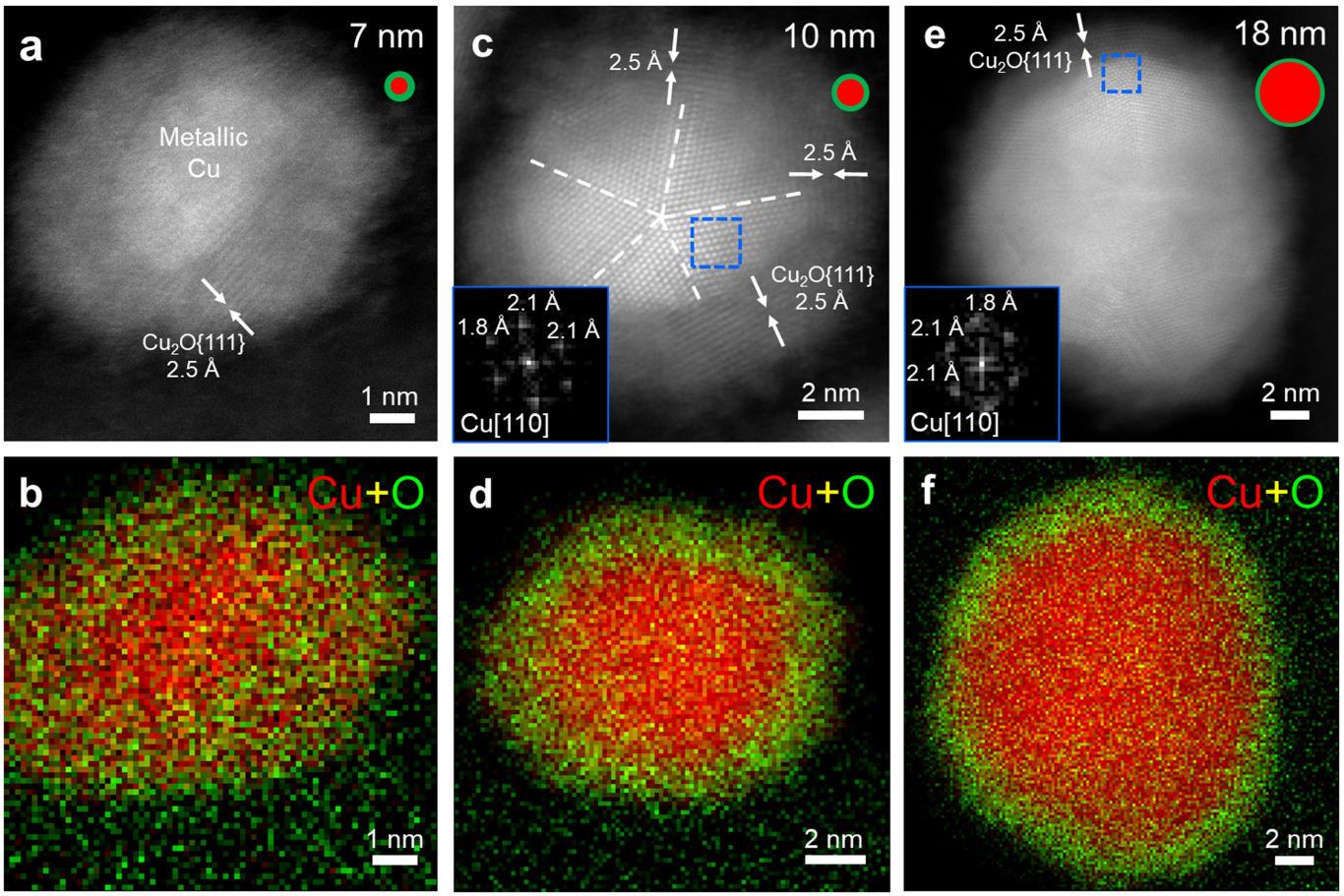

Extended Data Fig. 1 | Atomic-scale microstructures and chemical compositions of a family of Cu NP ensembles (7, 10, 18 nm). (**a**–**b**) HAADF-STEM image and EELS composite map of fresh 7 nm NPs with metallic Cu core (red) and ~2 nm oxide shell (green), which were oxidized to Cu_2O NPs after brief air exposure (Supplementary Fig. 3). (**c**) STEM image of 10 nm Cu@Cu_2O NPs with multi-domain Cu core close to the [110] zone axis surrounded by the Cu_2O shell with characteristic d-spacings of Cu_2O{111} (2.5 Å). (**d**) STEM-EELS composite map of 10 nm Cu@Cu_2O NPs with ~2 nm oxide shell. (**e**–**f**) STEM image of 18 nm Cu@Cu_2O NPs and EELS composite map showing the ~2 nm oxide shell.